

Unveiling the Spin–Valley Structure of Dipolar Exciton Ladders in R-stacked WSe₂/WS₂ Moiré Heterobilayers

Byeong Wook Cho,^{1,*} Tatyana V. Ivanova,^{1,*} Zhe Li,¹ Takashi Taniguchi,²
Kenji Watanabe,³ Brian D. Gerardot,^{1,†} and Mauro Brotons-Gisbert^{1,‡}

¹*Institute of Photonics and Quantum Sciences, SUPA, Heriot-Watt University, Edinburgh, UK.*

²*Research Center for Materials Nanoarchitectonics, National Institute for Materials Science, 1-1 Namiki, Tsukuba 305-0044, Japan*

³*Research Center for Electronic and Optical Materials, National Institute for Materials Science, 1-1 Namiki, Tsukuba 305-0044, Japan*

(Dated: July 9, 2026)

Localized interlayer excitons in moiré heterobilayers can form dipolar exciton ladders, yet their internal spin–valley structure remains unresolved. Here, we use helicity-resolved magnetophotoluminescence to identify the microscopic origin of the ladder in R-stacked WSe₂/WS₂ at charge neutrality and one-electron filling of the moiré lattice. At charge neutrality, the first two emission peaks correspond to a spin-triplet interlayer exciton and a triplet–triplet two-exciton state separated by 38 meV, reflecting the on-site dipolar interaction. The opposite Zeeman response of the apparent third rung of the ladder rules out its assignment as a spin-conserving three-exciton state and instead identifies it as a triplet–singlet two-exciton configuration with a 22 meV offset set by the WS₂ conduction-band spin splitting. At one-electron filling, the correlated electronic background gives rise to charged one- and two-exciton states and intervalley/intravalley two-exciton configurations, while reducing the effective exciton–exciton interaction. Our results establish a spin–valley-resolved picture of dipolar exciton ladders beyond simple occupation-number physics in moiré heterobilayers.

Moiré heterobilayers of transition-metal dichalcogenides (TMDs) provide a tunable platform for localizing interlayer excitons in periodic nanoscale potentials [1–5]. In type-II heterobilayers such as MoSe₂/WSe₂ and WSe₂/WS₂, electrons and holes reside in different layers, forming long-lived interlayer excitons (IXs) with permanent out-of-plane electric dipoles [6–21]. Moiré confinement makes these dipolar excitons optically addressable in both isolated and interacting regimes: at low exciton density, individual moiré traps can host isolated IXs that behave as quantum-dot-like emitters, whereas at higher density, multiple IXs can occupy and interact within the same moiré potential [8, 9, 22–24]. This combination of optical access, spatial confinement, and strong dipolar interactions makes moiré-trapped IXs a natural platform for exploring few- and many-body excitonic states.

In this high-density regime, dipolar interactions become prominent in the photoluminescence (PL) spectrum. The long-range component of the dipolar interaction continuously blueshifts the IX resonances, whereas the on-site component gives rise to discrete higher-energy emission peaks associated with successive IX occupation of a single moiré site, commonly interpreted as a dipolar exciton ladder [25–28]. In WSe₂/WS₂ moiré heterobilayers, the on-site Hubbard interaction between moiré-confined IXs reaches ~ 30 – 40 meV, far exceeding that reported in MoSe₂/WSe₂ systems (~ 2 meV) [25, 27]. This exceptionally large interaction energy makes WSe₂/WS₂ well suited for investigating excitonic Bose–Hubbard

physics [24, 29, 30]. Beyond its large interaction scale, the observed dipolar ladder also depends strongly on stacking geometry. Previous optical studies reported up to three resolved IX peaks in R-stacked samples, whereas only two were resolved in H-stacked configurations [25, 26]. This contrast has been attributed to their different real-space character: R-stacked IXs are vertically aligned and localized at a single registry, whereas H-stacked IXs are laterally displaced over multiple registries, leading to a more delocalized IX wavefunction [26, 31]. However, the unequal energy spacing of the three peaks observed in R-stacked WSe₂/WS₂ cannot be explained by on-site dipolar repulsion alone, indicating that additional internal degrees of freedom must be involved [25, 26].

Moreover, moiré-trapped IXs interact with correlated carriers introduced by electrostatic doping [32–35]. The resulting carrier–exciton interactions can shift IX resonance energies and generate additional excitonic complexes, whose microscopic nature remains poorly understood. A key missing ingredient in understanding both the charge-neutral and doped regimes is the internal spin–valley configuration of these IXs, inherited from the constituent TMD monolayers [36–38]. Because the accessible spin-split transitions and valley-dependent optical selection rules are determined by both the spin–valley configurations of the constituent TMD monolayers and the local atomic registry of the moiré site, multiple spin–valley-distinct IX states can contribute to the observed emission spectrum [8, 39, 40]. Resolving the spin–valley configurations of these excitonic states in R-stacked WSe₂/WS₂ is therefore essential to understand both the unequal spacing of the dipolar ladder at charge neutrality and the emergence of additional resonances in the presence of correlated carriers.

* These authors contributed equally to this work.

† B.D.Gerardot@hw.ac.uk

‡ m.brotons.i.gisbert@hw.ac.uk

In this Letter, we present a helicity-resolved magneto-optical study of moiré-confined IXs in R-stacked WSe_2/WS_2 heterobilayers as a function of exciton density and carrier filling ν . Here, ν denotes the number of excess carriers per moiré unit cell, with positive and negative values corresponding to electron and hole doping, respectively. At charge neutrality, we show that the exciton ladder cannot be understood as a simple sequence of spinless dipolar states. Instead, it comprises a spin-triplet ground-state interlayer exciton and two higher-energy two-exciton states with triplet–triplet and triplet–singlet spin–valley configurations. This microscopic assignment naturally explains the unequal ladder spacing through the spin-split WS_2 conduction band. At $\nu = 1$, the correlated electronic background reshapes the PL spectrum, giving rise to charged exciton–carrier complexes, charged two-exciton states, and a fine structure of intervalley and intravalley two-exciton configurations. Moreover, we observe a reduction of the effective inter-exciton dipolar repulsion at $\nu = 1$, demonstrating that resident electrons renormalize the interaction strength of bosonic excitons in the moiré lattice.

We fabricated three R-stacked WSe_2/WS_2 heterobilayer devices, R1–R3, using a dry-transfer method. The relative twist angles between WSe_2 and WS_2 were determined by polarization-resolved second-harmonic generation (SHG) measurements (see Supplemental Material, Sec. S1 and Fig. S1). All data presented in the main text were acquired from device R1. The devices employ a dual-gated geometry, enabling independent control of charge doping and out-of-plane electric field (see Supplemental Material, Sec. S2). PL measurements were performed at 3.9 K using a continuous-wave excitation laser at 1.680 eV, resonant with the $1s$ bright exciton state of WSe_2 , unless otherwise specified (see Supplemental Material, Fig. S2). Figure 1(a) shows a schematic of a dual-gated R-stacked WSe_2/WS_2 heterobilayer where electrons and holes are vertically aligned and localized at the same R_h^X moiré site, forming moiré-confined IXs with permanent out-of-plane dipole moments [25, 34]. Here, R_h^X denotes the R-type stacking with the chalcogen (X) site of the electron layer vertically aligned with the hexagon center (h) of the hole layer. This contrasts with H-stacked WSe_2/WS_2 , where the ground-state IX has a more extended real-space structure: one electron (hole) is localized near a moiré trap, while the wave function of the opposite hole (electron) is distributed over three symmetry-equivalent neighboring traps, giving the exciton an in-plane quadrupolar character in addition to its vertical dipole [31, 34]. In both stacking configurations, a single moiré site can host multiple IXs, which appear in PL spectra as successive emission peaks separated by the on-site dipolar repulsion, U_{dd} , with increasing exciton density. It has been suggested that the R-stacked WSe_2/WS_2 can support up to three IXs in a single moiré unit cell whereas the H-stacked configuration supports only two owing to its relatively delocalized IX nature [25, 26]. Figure 1(b) illustrates the relevant IX

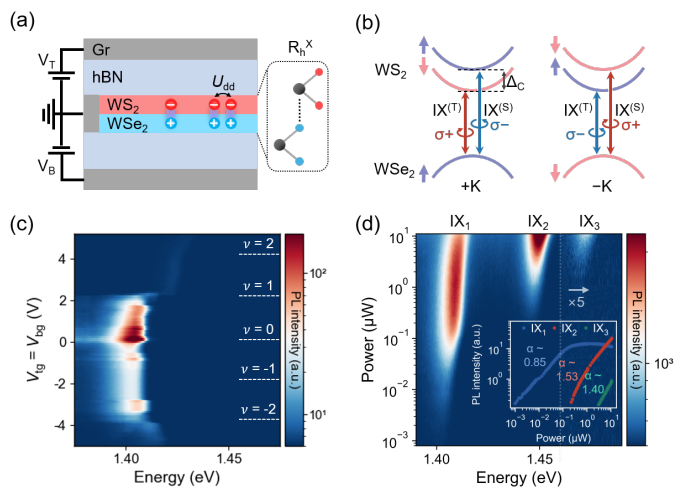


FIG. 1. (a) Schematic of the hBN-encapsulated dual-gated heterobilayer, where moiré-confined IXs carry out-of-plane electric dipoles and interact through on-site dipolar repulsion U_{dd} . (b) Spin–valley configurations and helicity-dependent optical selection rules for triplet $\text{IX}^{(T)}$ and singlet $\text{IX}^{(S)}$ transitions, separated by the WS_2 conduction-band spin splitting Δ_C . (c) Filling-dependent PL spectra measured at 10 nW under linearly polarized 1.680 eV excitation, showing systematic modulation of the IX emission with moiré lattice filling. (d) Excitation-power-dependent PL spectra at charge neutrality under the same excitation energy, showing the emergence of IX_2 and IX_3 above IX_1 . The high-energy spectral region is multiplied by a factor of five for clarity. Inset: integrated PL intensities of IX_1 , IX_2 , and IX_3 with power-law fits.

transitions in the R-stacked configuration, where the $+K$ ($-K$) valleys of WSe_2 and WS_2 are nearly aligned. The ground-state transition corresponds to the spin-triplet interlayer exciton ($\text{IX}^{(T)}$), while transitions involving the upper spin-split conduction band give rise to spin-singlet interlayer exciton ($\text{IX}^{(S)}$). These two states are separated by the conduction-band spin splitting, Δ_C (around 16–30 meV), and exhibit opposite circular polarization selection rules [39, 41–43] (see Supplemental Material, Sec. S3).

Figure 1(c) shows the filling-dependent PL spectra measured at an excitation power of 10 nW. The PL spectrum is dominated by the single-IX peak IX_1 , whose intensity and peak energy systematically change with moiré lattice filling. These lattice-filling-dependent PL modulations demonstrate the gate tunability of device R1. Here, we focus first on the charge-neutral regime, while carrier-induced modifications of the IX spectrum are discussed later in Fig. 4. Figure 1(d) shows the excitation power-dependent PL spectrum at charge neutrality ($\nu = 0$). At low excitation power, the emission is dominated by a single peak (IX_1) at 1.40 eV with a narrow linewidth of 11 meV (see Supplemental Material, Fig. S3). With increasing excitation power, IX_1 exhibits a continuous blueshift and its linewidth becomes narrower down to 8 meV at 140 nW. The blueshift is consistent with in-

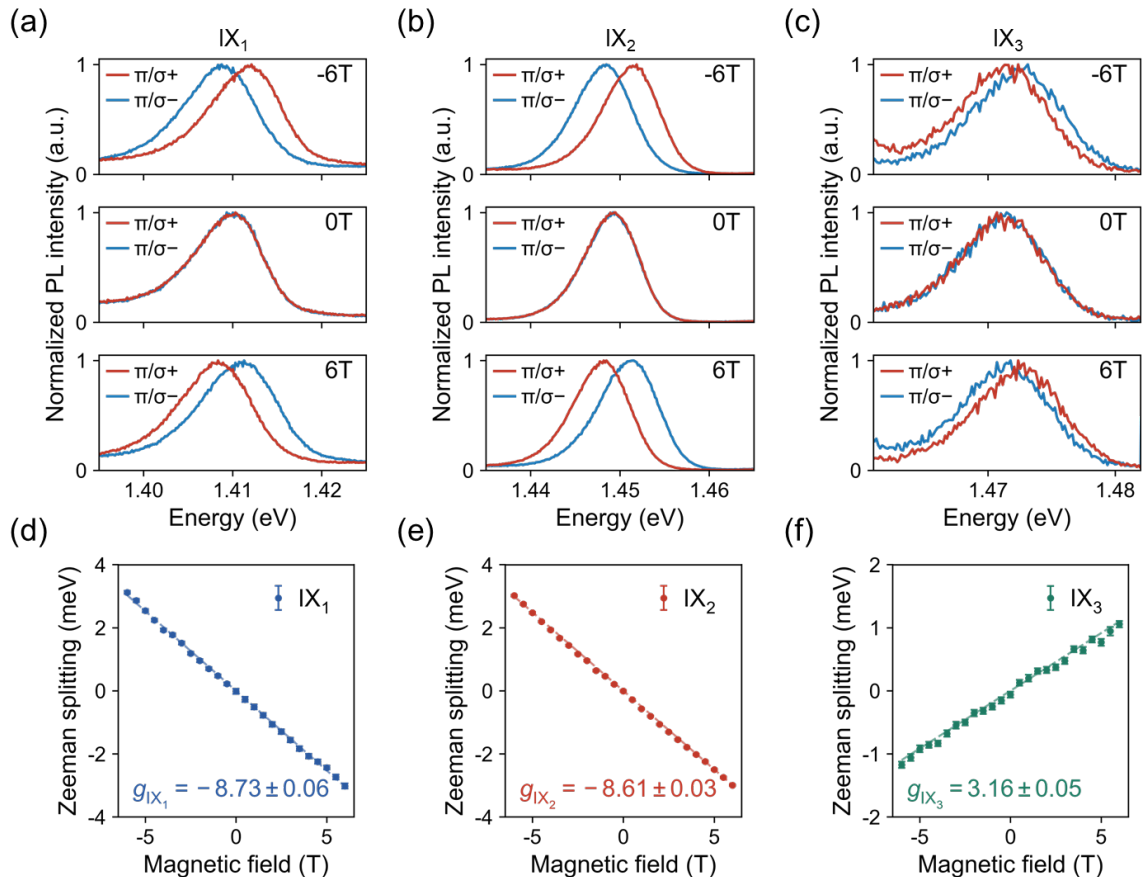


FIG. 2. (a–c) Helicity-resolved PL spectra of IX₁, IX₂, and IX₃ at representative magnetic fields ($B = -6, 0$, and $+6$ T), under linearly polarized 1.72 eV excitation with a power of $20 \mu\text{W}$. (d–f) Extracted Zeeman splitting, defined as $\Delta E = E_{\sigma^+} - E_{\sigma^-}$, as a function of magnetic field for IX₁, IX₂, and IX₃. Dashed lines are linear fits using $\Delta E = g\mu_B B$.

creasing long-range dipolar repulsion between IXs, while the linewidth narrowing suggests reduced disorder broadening as the exciton population approaches a bosonic Mott-like ordered configuration with nearly one IX per moiré site [26]. Above 140 nW, the linewidth of IX₁ broadens and a higher-energy peak, IX₂, emerges 38 meV above IX₁ (see Supplemental Material, Fig. S3). We assign IX₂ to a two-IX state localized at the same moiré site. This assignment is supported by the excitation-power dependence of the integrated PL intensities [44], shown in the inset of Fig. 1(d): IX₁ exhibits a sublinear scaling with an exponent of 0.85 and saturates near the onset of IX₂, whereas IX₂ shows a superlinear scaling with an exponent of 1.53. The energy separation between IX₂ and IX₁, denoted $\Delta E_{21} = 38$ meV, therefore represents the energy cost for two IXs to occupy the same moiré site, corresponding to the on-site dipolar repulsion U_{dd} . At higher excitation powers ($3 \mu\text{W}$), a third emission peak (IX₃) appears near 1.47 eV. Although IX₃ has previously been attributed to a three-exciton state within a single moiré site, its separation from IX₂, $\Delta E_{32} = 22$ meV, is substantially smaller than $\Delta E_{21} = 38$ meV [25, 26]. This reduced spacing is incon-

sistent with a simple dipolar ladder in which IX₃ represents a three-IX state. Moreover, the power-law exponent of IX₃ is 1.40, slightly smaller than that of IX₂. We therefore attribute IX₃ to a two-exciton state with a spin–valley configuration distinct from that of IX₂. Similar power-dependent intensity evolution and energy hierarchy of IX₁–IX₃ are observed in devices R2 and R3 (see Supplemental Material, Fig. S4).

We performed helicity-resolved PL measurements under out-of-plane magnetic fields to investigate the origin of IX₃. Figures 2(a)–2(c) show normalized σ^+ - and σ^- -resolved PL spectra of IX₁, IX₂, and IX₃, respectively, measured under linearly polarized 1.72 eV excitation at representative out-of-plane magnetic fields ($B = -6, 0$, and $+6$ T; see Supplemental Material, Fig. S5 for the full magnetic-field-dependent spectra). The applied magnetic field lifts the valley degeneracy through the Zeeman effect, producing opposite energy shifts for excitonic transitions in the $+K$ and $-K$ valleys and thereby enabling identification of their spin–valley configurations [45, 46]. For each magnetic field, we extract the fitted PL peak energies E_{σ^+} and E_{σ^-} from the σ^+ and σ^- detection channels, respectively. The Zeeman splitting is then de-

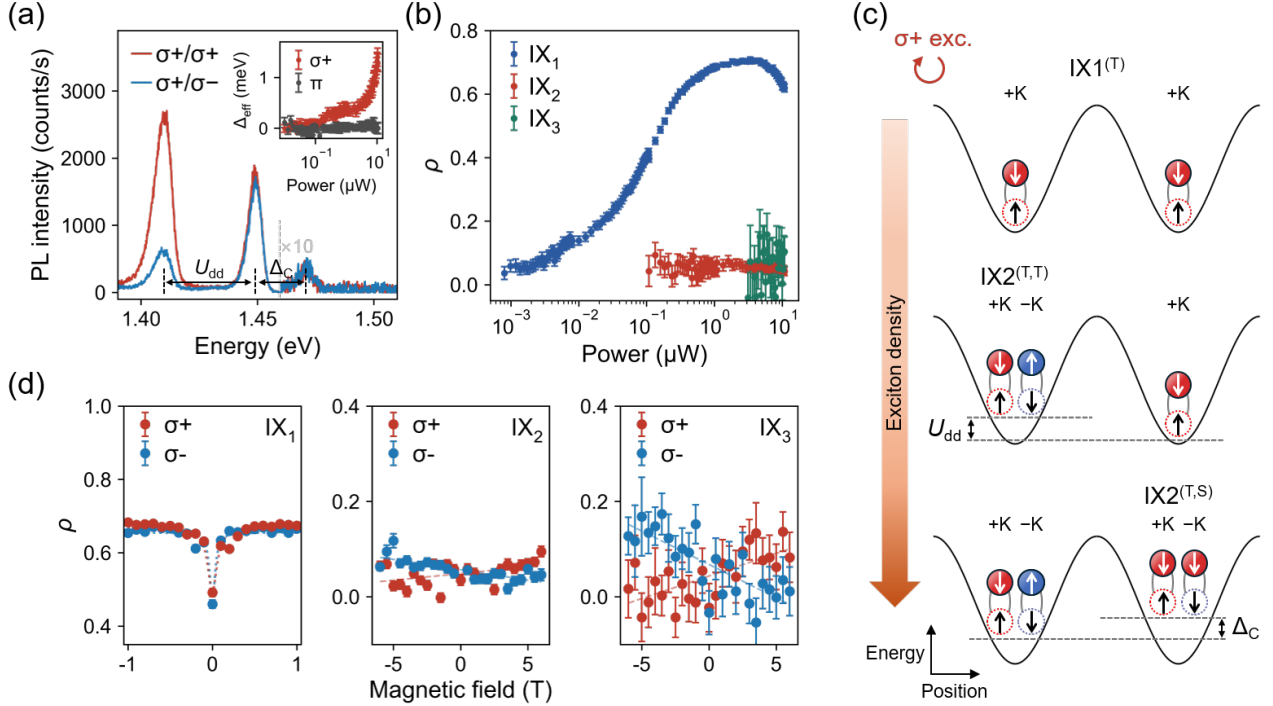


FIG. 3. (a) Helicity-resolved PL spectra measured under σ^+ excitation with a power of $7 \mu\text{W}$. The high-energy IX_3 region is multiplied by a factor of 10 for clarity. The inset compares the IX_1 splitting under linearly polarized and σ^+ excitation, highlighting the excitation-helicity-induced energy splitting. (b) Degree of circular polarization (ρ) of IX_1 , IX_2 , and IX_3 as a function of excitation power. (c) Schematic potential-energy landscape of the IX population dynamics under σ^+ excitation at charge neutrality. Increasing excitation density enhances the valley imbalance of $\text{IX}_1^{(\text{T})}$ and is accompanied by the formation of intervalley two-exciton states, yielding $\text{IX}_2^{(\text{T},\text{T})}$ and $\text{IX}_2^{(\text{T},\text{S})}$ with negligible net valley polarization. (d) Magnetic-field dependence of ρ for IX_1 , IX_2 , and IX_3 under σ^+ and σ^- excitation.

defined as $\Delta E = E_{\sigma^+} - E_{\sigma^-} = g\mu_B B$, where g is the effective exciton g -factor and μ_B is the Bohr magneton. Figures 2(d)–2(f) show the extracted energy splittings versus magnetic field, together with linear fits. IX_1 exhibits a g -factor of $g_{\text{IX}_1} = -8.73 \pm 0.06$, consistent with previously reported values for the $\text{IX}^{(\text{T})}$ in R-stacked WSe_2/WS_2 [47]. IX_2 shows a nearly identical g -factor of $g_{\text{IX}_2} = -8.61 \pm 0.03$, indicating that the corresponding two-IX state retains the same triplet optical transition. In contrast, IX_3 exhibits a g -factor of $g_{\text{IX}_3} = 3.16 \pm 0.05$, with opposite sign and significantly reduced magnitude. This value is consistent with expectations for the $\text{IX}^{(\text{S})}$, as estimated within a single-particle framework including spin, atomic orbital, and Berry-curvature contributions (see Supplemental Material, Sec. S4 and Fig. S6) [36, 48]. The same single-particle framework also captures the g -factors of IX_1 and IX_2 , supporting the assignment of IX_3 to a transition involving $\text{IX}^{(\text{S})}$. Together with the nearly quadratic power dependence relative to IX_1 and the energy separation ΔE_{32} comparable to the WS_2 conduction-band spin splitting Δ_C , these results indicate that IX_3 originates from a two-exciton state composed of one $\text{IX}^{(\text{T})}$ and one $\text{IX}^{(\text{S})}$ confined in the same moiré site.

Figure 3(a) compares PL spectra measured at $7 \mu\text{W}$ in co- and cross-circular excitation-detection configura-

tions, providing access to the spin-valley configurations of the observed IX peaks. The polarization response of the optical setup was calibrated to remove systematic helicity-dependent detection asymmetries (see Supplemental Material, Sec. S5 and Fig. S7). As reported previously [25, 26, 47], IX_1 exhibits strong co-circular polarization with respect to the excitation helicity (Fig. 3(b)). We quantify the degree of circular polarization as $\rho = (I_{\text{co}} - I_{\text{cross}})/(I_{\text{co}} + I_{\text{cross}})$, where I_{co} and I_{cross} are the integrated PL intensities of the corresponding IX peak in the co- and cross-circular detection channels, respectively. For IX_1 , ρ increases with excitation power and approaches 0.7 near $2 \mu\text{W}$. We also observe a small energy splitting, $\Delta_{\text{eff}} = E_{\text{co}} - E_{\text{cross}}$, between the co- and cross-circular emission channels of IX_1 , with $E_{\text{co}} > E_{\text{cross}}$. This splitting increases with excitation power and is attributed to a valley population imbalance between the $+K$ and $-K$ valleys [49] (see the inset of Fig. 3(a)). This helicity-induced energy mismatch between the two valley configurations can suppress exchange-mediated valley mixing, leading to an enhanced ρ of IX_1 at elevated excitation powers. At excitation powers above $5 \mu\text{W}$, the IX_1 polarization gradually decreases, which we attribute to exciton dissociation and enhanced intervalley scattering at high IX densities. This reduction

is consistent with the decrease of the IX_1 PL intensity in the same high-power regime (see the inset of Fig. 1(d)). In contrast, ρ for IX_2 remains nearly zero over the investigated excitation-power range. This nearly vanishing circular polarization is consistent with our assignment of IX_2 to an intervalley two-exciton state composed of one $IX^{(T)}$ in the $+K$ valley and the other $IX^{(T)}$ in the $-K$ valley, or vice versa, for which the two circular emission pathways are nearly indistinguishable [25]. Such an intervalley configuration is energetically favored because the exchange interaction is reduced for anti-aligned spin-valley configurations. We further note that ρ for IX_1 increases more rapidly above the onset of IX_2 . This observation is consistent with a scenario in which IX_2 forms preferentially from opposite-valley excitons, thereby reducing the cross-polarized IX population and increasing ρ for IX_1 [47]. Similarly, IX_3 exhibits a nearly zero ρ over the investigated excitation-power range, indicating that it also involves an intervalley two-IX configuration rather than a co-circularly polarized intravalley state. Together with the opposite-sign g -factor of IX_3 discussed above, the nearly vanishing ρ supports its assignment to an intervalley triplet-singlet two-IX configuration. Based on these observations, we identify IX_1 , IX_2 , and IX_3 as a triplet interlayer exciton, $IX_1^{(T)}$, a triplet-triplet two-exciton state, $IX_2^{(T,T)}$, and a triplet-singlet two-exciton state, $IX_2^{(T,S)}$, respectively (Fig. 3(c)). Here, the number following IX denotes the number of constituent excitons, while the superscripts denote their spin character.

Figure 3(d) shows the ρ of IX_1 , IX_2 , and IX_3 as a function of out-of-plane magnetic field. The polarization of IX_1 was measured at 150 nW, for which the zero-field polarization remains unsaturated. For both σ^+ and σ^- excitation, the polarization increases sharply with magnetic field, reaching 0.7 at $B_c \approx 0.05$ T before saturating. This characteristic field is comparable to values previously reported for R-stacked WSe_2/WS_2 heterobilayers [47] (see Supplemental Material, Sec. S6 for the fitting procedure). This behavior is attributed to the magnetic-field-induced lifting of the $+K/-K$ valley degeneracy, which suppresses electron-hole-exchange-driven depolarization [47, 50]. A residual depolarization of about 0.3 persists even at high magnetic fields and high excitation powers, while the saturation field remains similar across the investigated excitation-power range (see Supplemental Material, Fig. S8). This residual depolarization is likely due to the long IX lifetime, which allows depolarizing channels to remain effective even when exchange-induced valley mixing is partially suppressed [51, 52]. Since an out-of-plane magnetic field lifts the valley degeneracy, it could in principle modify the valley population balance and thus the polarization of intervalley two-exciton states. However, IX_2 shows negligible ρ throughout the investigated magnetic-field range, indicating that its two intervalley emission pathways remain nearly symmetric.

By contrast, IX_3 exhibits a field- and excitation-helicity-dependent polarization response. In our assign-

ment, IX_3 arises from recombination of the spin-singlet component of an intervalley two exciton configuration, composed of $IX^{(T)}$ in one valley and $IX^{(S)}$ in the opposite valley (Fig. 3(c)). According to the selection rules in Fig. 1(b), σ^+ (σ^-) excitation addresses the $IX^{(S)}$ transition in the $-K$ ($+K$) valley. The observed helicity dependence therefore indicates that the higher-energy valley branch develops a larger ρ than the lower-energy branch. A related behavior has been reported for bright spin-singlet excitons in monolayer WSe_2 , where an out-of-plane magnetic field modifies the valley-dependent exciton dispersion through electron-hole exchange interactions [53]. In that case, the magnetic field lifts the valley degeneracy and separates the exchange-coupled exciton branches, favoring radiative recombination from the upper branch. Although the spatially indirect character of IX_3 is expected to substantially reduce both the exchange interaction and oscillator strength, the spin-singlet recombination channel may retain a similar exchange-mediated polarization mechanism. Such a scenario could account for the distinct magnetic-field-dependent polarization response of IX_3 .

Having identified the spin-valley configurations of the charge-neutral exciton ladder, we next examine how resident carriers reshape the dipolar exciton spectrum. Figure 4(a) shows filling-dependent PL spectra measured at 7 μ W over the range from one hole per moiré site ($\nu = -1$) to one electron per moiré site ($\nu = 1$) (see Supplemental Material, Fig. S9 for the full filling-dependent spectra). Representative linecuts at $\nu = -1, 0$, and 1 are shown in Fig. 4(b), displaying the asymmetric evolution of the IX ladder under hole and electron doping. On the hole-doped side, IX_1 weakly blueshifts by approximately 6 meV at $\nu = -1$, while IX_2 gradually loses oscillator strength and separates into two peaks with distinct energies beyond $\nu = -1$ (see Supplemental Material, Sec. S7 for a detailed discussion of the hole-doped regime). We focus below on the electron-doped regime, where additional resonances emerge most prominently near $\nu = 1$.

As the moiré lattice is populated with electrons, a new emission peak, IX'_1 , emerges approximately 13 meV above IX_1 . We assign IX'_1 to a charged exciton-carrier complex, $IX_1^{(T)} + e$, formed by the interaction between a moiré-trapped triplet IX and a resident electron occupying the same moiré site (Fig. 4(c)) [25, 32, 33]. The intensity of IX'_1 increases as ν approaches 1, consistent with the growing population of localized electron-exciton complexes. The behavior of IX_2 is markedly different. Although its intensity is strongly modulated by electron filling, its emission energy remains close to that of the charge-neutral IX_2 even at $\nu = 1$. We therefore denote this resonance as IX'_2 . By contrast, IX_3 rapidly loses oscillator strength upon both electron and hole doping, indicating that the singlet-derived two-IX channel is strongly suppressed by the presence of resident carriers. At $\nu = 1$, the PL spectrum consists of IX'_1 , IX'_2 , and two additional resonances at 1.461 eV and 1.483 eV, denoted IX'_3 and IX'_4 , respectively. These two peaks are observed

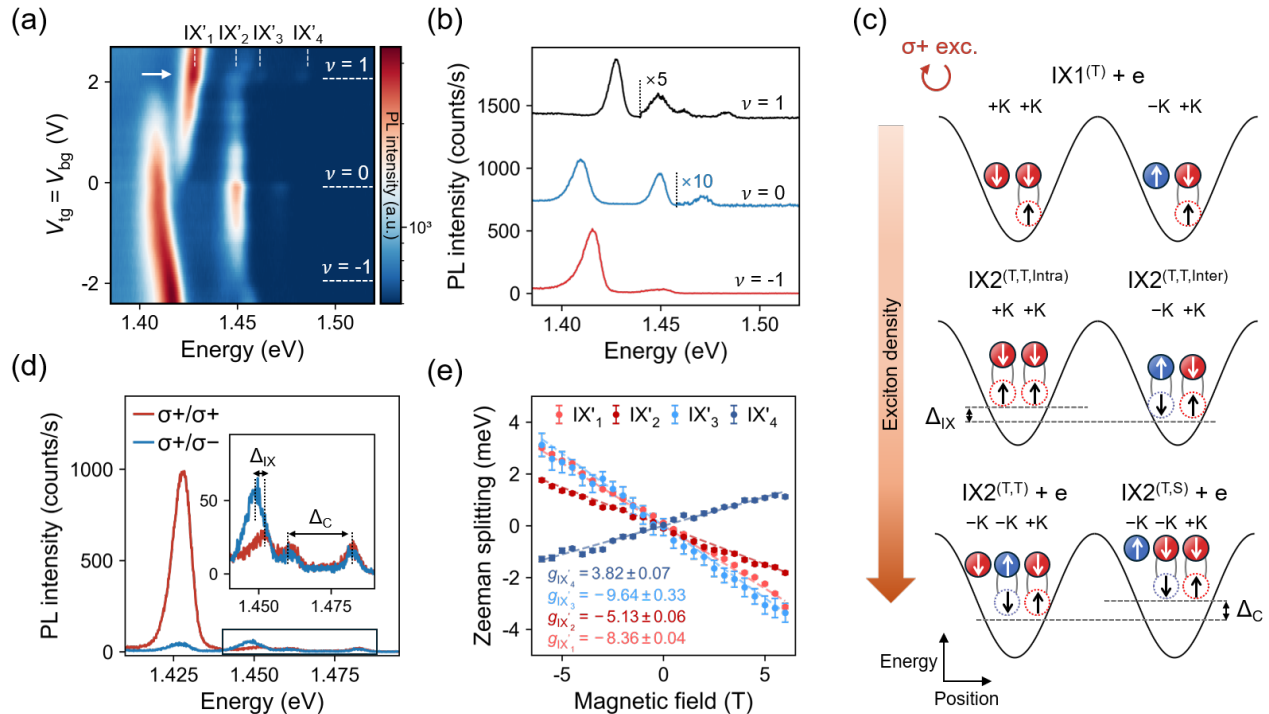


FIG. 4. (a) Filling-dependent PL spectra measured at $7 \mu\text{W}$ under linearly polarized 1.680 eV excitation, showing the evolution of the IX emission from hole to electron filling. Additional resonances $\text{IX}'_1\text{--}\text{IX}'_4$ emerge prominently near $\nu = 1$. (b) Representative linecuts at $\nu = -1, 0$, and 1 . The high-energy spectral region is multiplied for clarity. (c) Schematic potential-energy landscape of the IX population dynamics under σ^+ excitation at $\nu = 1$. (d) Helicity-resolved PL spectra at $\nu = 1$ under σ^+ excitation. (e) Zeeman splittings of $\text{IX}'_1\text{--}\text{IX}'_4$ as a function of out-of-plane magnetic field.

prominently only near $\nu = 1$, suggesting that they are closely tied to the correlated electronic background established at one electron per moiré site.

Figure 4(d) shows helicity-resolved PL spectra at $\nu = 1$ under σ^+ excitation. Similar to IX_1 at charge neutrality, IX'_1 exhibits strongly co-circularly polarized emission, with ρ approaching 0.9. This enhanced polarization of IX'_1 compared with charge-neutral IX_1 ($\rho \sim 0.7$) may arise from the shorter lifetime of the charged excitonic complex, which suppresses exchange-mediated valley depolarization [47, 51]. Strikingly, IX'_2 exhibits strong cross-circular polarization, in contrast to charge-neutral IX_2 , which is nearly unpolarized (Fig. 3(b)). Moreover, the co-circular component of IX'_2 appears at a slightly higher energy than the cross-circular component, with an energy splitting of $\sim 2.8 \text{ meV}$ (inset of Fig. 4(d)). Neither the ρ nor the energy splitting is observed under linearly polarized excitation, indicating that both originate from optically induced valley-selective populations (see Supplemental Material, Fig. S10).

The proximity of IX'_2 to the charge-neutral IX_2 resonance suggests that it retains a neutral two-exciton-like character, rather than forming a completely distinct charged excitonic complex. We therefore attribute the lower- and higher-energy components of IX'_2 to intervalley and intravalley $\text{IX}2^{(\text{T},\text{T})}$ configurations, respectively, as illustrated in Fig. 4(c). Under σ^+ excitation reso-

nant with the WSe_2 $1s$ exciton, K -valley $\text{IX}^{(\text{T})}$ states are preferentially generated. Because the electronic background at $\nu = 1$ is not known to be valley polarized in WSe_2/WS_2 [1, 25], the preexisting electrons may occupy either the $+K$ or $-K$ valley. When a resident electron participates in the formation of a second $\text{IX}^{(\text{T})}$ in the same valley as the optically generated IX, an intravalley ($+K, +K$) two-exciton configuration is realized. By contrast, participation of an electron from the opposite valley leads to an intervalley two-exciton configuration ($+K, -K$). The lower energy of the cross-circular component is consistent with the intervalley configuration being energetically favored over the intravalley one. The stronger cross-circular polarization of IX'_2 further suggests that this lower-energy intervalley channel is preferentially populated under circularly polarized excitation. The observed splitting is comparable to the intravalley–intervalley two-exciton splitting reported in H-stacked WSe_2/WS_2 [54], supporting our assignment to intervalley and intravalley two-IX configurations.

We next consider the origin of IX'_3 and IX'_4 . Both peaks are nearly unpolarized, similar to IX_2 and IX_3 at charge neutrality. One possible interpretation is that they originate from moiré trapping sites with a different atomic registry. This scenario is unlikely, however, since the calculated energy offset between the R_h^X site and the next local minimum is expected to be on the order of

~ 100 meV or larger [10, 55], whereas IX'_3 and IX'_4 lie only 52 meV and 74 meV above IX_1 , respectively. Consistent with this picture, the out-of-plane electric-field dependence of IX'_1 – IX'_4 yields similar electron–hole separations of ~ 0.7 nm from the measured DC Stark shifts, indicating that all four peaks originate from the moiré sites with the same local atomic registry (Fig. S11). The excitation-power-dependent PL intensity further supports a many-body origin for IX'_3 and IX'_4 . Both IX'_3 and IX'_4 emerge at higher onset powers than IX'_1 and IX'_2 and exhibit strongly nonlinear power-law scaling, with exponents of $\alpha \sim 3.4$ and 4.0, respectively (Fig. S12). These large exponents suggest that IX'_3 and IX'_4 emerge through higher-order formation pathways in the correlated electron–IX background, following the sequential occupation of lower-energy charged IX states.

The energy hierarchy closely mirrors that of the charge-neutral IX ladder. The energy separations between IX'_1 and IX'_3 , and between IX'_3 and IX'_4 , are approximately 34 meV and 22 meV, respectively, comparable to the corresponding energy separations between IX_1 , IX_2 , and IX_3 at $\nu = 0$. Furthermore, helicity-resolved magneto-PL measurements reveal distinct Zeeman responses for IX'_3 and IX'_4 (Fig. 4(e)). The extracted g -factors are $g_{IX'_3} = -9.64 \pm 0.33$ and $g_{IX'_4} = 3.82 \pm 0.07$, respectively, closely matching those of $IX2^{(T,T)}$ and $IX2^{(T,S)}$ at charge neutrality. The modest renormalization of g -factors relative to the neutral case may arise from exchange interactions within the electron–exciton complex [56]. Taken together, these observations identify IX'_3 and IX'_4 as charged two-exciton states, $IX2^{(T,T)} + e$ and $IX2^{(T,S)} + e$, respectively (Fig. 4(c)). Their emergence only in the vicinity of $\nu = 1$ indicates that they originate from interactions between multiple IXs and a localized electron embedded in the correlated electronic background [4]. Thus, the resident electron acts as a localized fermionic degree of freedom coupled to the bosonic dipolar ladder. We finally note that the energy separation between IX'_1 and IX'_3 is around 34 meV, slightly smaller than the charge-neutral on-site dipolar

repulsion $U_{dd} \sim 38$ meV. The reduction indicates that the resident electron partially screens the IX–IX interaction, leading to a renormalization of the effective dipolar repulsion within the moiré lattice.

In summary, we identify the spin–valley configurations of multiple moiré-confined IX states in R-stacked WSe_2/WS_2 heterobilayers. Polarization-resolved magneto-PL measurements reveal that the observed peaks do not form a simple dipolar ladder generated solely by the successive occupation of the ground-state $IX^{(T)}$ excitons. Instead, the spin-split WS_2 conduction band gives rise to distinct triplet–triplet and triplet–singlet two-exciton configurations, establishing the microscopic origin of the unequal ladder spacing at charge neutrality. At electron filling $\nu = 1$, the correlated electronic background reshapes the emission spectrum, giving rise to charged electron–IX complexes and reducing the effective interaction energy of the dipolar ladder. We further observe a helicity-dependent fine structure of the two-IX emission, consistent with the coexistence of inter-valley and intravalley configurations. Our results establish TMD heterobilayers as a promising platform for exploring spin-dependent Bose–Fermi mixtures, where the spin–valley degrees of freedom of excitons and resident carriers jointly determine the formation of correlated excitonic complexes.

ACKNOWLEDGMENTS

This work was supported by the EPSRC (grant nos. EP/P029892/1 and EP/Y026284/1). B. W. C. is supported by a Marie Skłodowska-Curie Individual Fellowship (No. 101208787). M.B.-G. is supported by a Royal Society University Research Fellowship. B.D.G. is supported by a Chair in Emerging Technology from the Royal Academy of Engineering. K.W. and T.T. acknowledge the support from the JSPS KAKENHI (Grant Numbers 21H05233 and 23H02052), the CREST (JPMJCR24A5), JST and World Premier International Research Center Initiative (WPI), MEXT, Japan.

-
- [1] Y. Tang, L. Li, T. Li, Y. Xu, S. Liu, K. Barmak, K. Watanabe, T. Taniguchi, A. H. MacDonald, J. Shan, and K. F. Mak, Simulation of Hubbard model physics in WSe_2/WS_2 moiré superlattices, *Nature* **579**, 353 (2020), 27.
 - [2] F. Wu, T. Lovorn, E. Tutuc, and A. H. MacDonald, Hubbard model physics in transition metal dichalcogenide moiré bands, *Physical Review Letters* **121**, 026402 (2018), 23, 1804.03151.
 - [3] C. Jin, E. C. Regan, A. Yan, M. I. B. Utama, D. Wang, S. Zhao, Y. Qin, S. Yang, Z. Zheng, S. Shi, K. Watanabe, T. Taniguchi, S. Tongay, A. Zettl, and F. Wang, Observation of moiré excitons in WSe_2/WS_2 heterostructure superlattices, *Nature* **567**, 76 (2019), 28, 1812.09815.
 - [4] E. C. Regan, D. Wang, C. Jin, M. I. B. Utama, B. Gao, X. Wei, S. Zhao, W. Zhao, Z. Zhang, K. Yumigeta, M. Blei, J. D. Carlström, K. Watanabe, T. Taniguchi, S. Tongay, M. Crommie, A. Zettl, and F. Wang, Mott and generalized Wigner crystal states in WSe_2/WS_2 moiré superlattices, *Nature* **579**, 359 (2020), 29, 1910.09047.
 - [5] E. Liu, T. Taniguchi, K. Watanabe, N. M. Gabor, Y.-T. Cui, and C. H. Lui, Excitonic and valley-polarization signatures of fractional correlated electronic phases in a WSe_2/WS_2 moiré superlattice, *Physical Review Letters* **127**, 037402 (2021), 64, 2011.13892.
 - [6] P. Rivera, J. R. Schaibley, A. M. Jones, J. S. Ross, S. Wu, G. Aivazian, P. Klement, K. Seyler, G. Clark, N. J. Ghimire, J. Yan, D. G. Mandrus, W. Yao, and X. Xu, Observation of long-lived interlayer excitons in monolayer $MoSe_2$ – WSe_2 heterostructures, *Nature Communications*

- 6**, 6242 (2015), 07,32, 1403.4985.
- [7] R. Xiong, J. H. Nie, S. L. Brantly, P. Hays, R. Sailus, K. Watanabe, T. Taniguchi, S. Tongay, and C. Jin, Correlated insulator of excitons in WSe_2/WS_2 moiré superlattices, *Science* **380**, 860 (2023), 2207.10764.
- [8] M. Brotons-Gisbert, H. Baek, A. Campbell, K. Watanabe, T. Taniguchi, and B. D. Gerardot, Moiré-trapped interlayer trions in a charge-tunable $\text{WSe}_2/\text{MoSe}_2$ heterobilayer, *Physical Review X* **11**, 031033 (2021), 2101.07747.
- [9] E. Liu, E. Barré, J. v. Baren, M. Wilson, T. Taniguchi, K. Watanabe, Y.-T. Cui, N. M. Gabor, T. F. Heinz, Y.-C. Chang, and C. H. Lui, Signatures of moiré trions in $\text{WSe}_2/\text{MoSe}_2$ heterobilayers, *Nature* **594**, 46 (2021).
- [10] L. Yuan, B. Zheng, J. Kunstmann, T. Brumme, A. B. Kuc, C. Ma, S. Deng, D. Blach, A. Pan, and L. Huang, Twist-angle-dependent interlayer exciton diffusion in $\text{WS}_2\text{-WSe}_2$ heterobilayers, *Nature Materials* **19**, 617 (2020), 1910.02869.
- [11] Z. Zhang, E. C. Regan, D. Wang, W. Zhao, S. Wang, M. Sayyad, K. Yumigeta, K. Watanabe, T. Taniguchi, S. Tongay, M. Crommie, A. Zettl, M. P. Zaletel, and F. Wang, Correlated interlayer exciton insulator in heterostructures of monolayer WSe_2 and moiré WS_2/WSe_2 , *Nature Physics* **18**, 1214 (2022), 2108.07131.
- [12] H. Fang, Q. Lin, Y. Zhang, J. Thompson, S. Xiao, Z. Sun, E. Malic, S. P. Dash, and W. Wiczorek, Localization and interaction of interlayer excitons in $\text{MoSe}_2/\text{WSe}_2$ heterobilayers, *Nature Communications* **14**, 6910 (2023), 2307.03842.
- [13] X. Wang, J. Zhu, K. L. Seyler, P. Rivera, H. Zheng, Y. Wang, M. He, T. Taniguchi, K. Watanabe, J. Yan, D. G. Mandrus, D. R. Gamelin, W. Yao, and X. Xu, Moiré trions in $\text{MoSe}_2/\text{WSe}_2$ heterobilayers, *Nature Nanotechnology* **16**, 1208 (2021).
- [14] M. Förg, L. Colombier, R. K. Patel, J. Lindlau, A. D. Mohite, H. Yamaguchi, M. M. Glazov, D. Hunger, and A. Högele, Cavity-control of interlayer excitons in van der Waals heterostructures, *Nature Communications* **10**, 3697 (2019), 1710.00990.
- [15] C. Qian, M. Troue, J. Figueiredo, P. Soubelet, V. Villafañe, J. Beierlein, S. Klembt, A. V. Stier, S. Höfling, A. W. Holleitner, and J. J. Finley, Lasing of moiré trapped $\text{MoSe}_2/\text{WSe}_2$ interlayer excitons coupled to a nanocavity, *Science Advances* **10**, eadk6359 (2024), 2302.07046.
- [16] Y. Liu, H. Fang, A. Rasmita, Y. Zhou, J. Li, T. Yu, Q. Xiong, N. Zheludev, J. Liu, and W. Gao, Room temperature nanocavity laser with interlayer excitons in 2D heterostructures, *Science Advances* **5**, eaav4506 (2019).
- [17] S. Zhao, Z. Li, X. Huang, A. Rupp, J. Göser, I. A. Vovk, S. Y. Kruchinin, K. Watanabe, T. Taniguchi, I. Bilgin, A. S. Baimuratov, and A. Högele, Excitons in mesoscopically reconstructed moiré heterostructures, *Nature Nanotechnology* **18**, 572 (2023), 2202.11139.
- [18] F. Tagarelli, E. Lopriore, D. Erkensten, R. Perea-Causín, S. Brem, J. Hagel, Z. Sun, G. Pasquale, K. Watanabe, T. Taniguchi, E. Malic, and A. Kis, Electrical control of hybrid exciton transport in a van der Waals heterostructure, *Nature Photonics* **17**, 615 (2023), 2303.00419.
- [19] N. R. Wilson, P. V. Nguyen, K. Seyler, P. Rivera, A. J. Marsden, Z. P. L. Laker, G. C. Constantinescu, V. Kandyba, A. Barinov, N. D. M. Hine, X. Xu, and D. H. Cobden, Determination of band offsets, hybridization, and exciton binding in 2D semiconductor heterostructures, *Science Advances* **3**, e1601832 (2017), 10.
- [20] M. Troue, J. Figueiredo, L. Sigl, C. Paspalides, M. Katzer, T. Taniguchi, K. Watanabe, M. Selig, A. Knorr, U. Wurstbauer, and A. W. Holleitner, Extended spatial coherence of interlayer excitons in $\text{MoSe}_2/\text{WSe}_2$ heterobilayers, *Physical Review Letters* **131**, 036902 (2023), 2302.10312.
- [21] L. A. Jauregui, A. Y. Joe, K. Pistunova, D. S. Wild, A. A. High, Y. Zhou, G. Scuri, K. D. Greve, A. Sushko, C.-H. Yu, T. Taniguchi, K. Watanabe, D. J. Needleman, M. D. Lukin, H. Park, and P. Kim, Electrical control of interlayer exciton dynamics in atomically thin heterostructures, *Science* **366**, 870 (2019), 1812.08691.
- [22] K. L. Seyler, P. Rivera, H. Yu, N. P. Wilson, E. L. Ray, D. G. Mandrus, J. Yan, W. Yao, and X. Xu, Signatures of moiré-trapped valley excitons in $\text{MoSe}_2/\text{WSe}_2$ heterobilayers, *Nature* **567**, 66 (2019), 39, 1809.04562.
- [23] H. Baek, M. Brotons-Gisbert, Z. X. Koong, A. Campbell, M. Rambach, K. Watanabe, T. Taniguchi, and B. D. Gerardot, Highly energy-tunable quantum light from moiré-trapped excitons, *Science Advances* **6**, eaba8526 (2020), 37.
- [24] H. Yu, G.-B. Liu, J. Tang, X. Xu, and W. Yao, Moiré excitons: From programmable quantum emitter arrays to spin-orbit-coupled artificial lattices, *Science Advances* **3**, e1701696 (2017), 1710.07015.
- [25] H. Park, J. Zhu, X. Wang, Y. Wang, W. Holtzmann, T. Taniguchi, K. Watanabe, J. Yan, L. Fu, T. Cao, D. Xiao, D. R. Gamelin, H. Yu, W. Yao, and X. Xu, Dipole ladders with large Hubbard interaction in a moiré exciton lattice, *Nature Physics* **19**, 1286 (2023).
- [26] Z. Lian, Y. Meng, L. Ma, I. Maity, L. Yan, Q. Wu, X. Huang, D. Chen, X. Chen, X. Chen, M. Blei, T. Taniguchi, K. Watanabe, S. Tongay, J. Lischner, Y.-T. Cui, and S.-F. Shi, Valley-polarized excitonic Mott insulator in WS_2/WSe_2 moiré superlattice, *Nature Physics* **20**, 34 (2024).
- [27] W. Li, X. Lu, S. Dubey, L. Devenica, and A. Srivastava, Dipolar interactions between localized interlayer excitons in van der Waals heterostructures, *Nature Materials* **19**, 624 (2020), 1910.08139.
- [28] L. Huang, C. Ge, B. Xu, Y. Wang, S. Li, X. Luo, H. Zhao, D. Zhang, Z. Zeng, Q. Tong, D. Li, X. Zhu, K. Braun, T. Gao, X. Wang, and A. Pan, Moiré-orbital-resolved excitonic Mott insulating states and their optical and electric control in van der Waals heterostructures, *Physical Review Letters* **135**, 096902 (2025).
- [29] N. Götting, F. Lohof, and C. Gies, Moiré-Bose-Hubbard model for interlayer excitons in twisted transition metal dichalcogenide heterostructures, *Physical Review B* **105**, 165419 (2022), 2201.10877.
- [30] B. Gao, D. G. Suárez-Forero, S. Sarkar, T.-S. Huang, D. Session, M. J. Mehrabad, R. Ni, M. Xie, P. Upadhyay, J. Vannucci, S. Mittal, K. Watanabe, T. Taniguchi, A. Imamoglu, Y. Zhou, and M. Hafezi, Excitonic Mott insulator in a Bose-Fermi-Hubbard system of moiré WS_2/WSe_2 heterobilayer, *Nature Communications* **15**, 2305 (2024), 2304.09731.
- [31] L. M. Devenica, Z. Hadjri, J. Kumlin, D. Suárez-Forero, R. Li, K. Domi, B. Lyu, W. Li, L. Fausten, V. Vento, N. Ubrig, S. Liu, J. Hone, K. Watanabe, T. Taniguchi, T. Pohl, and A. Srivastava, Collective photon emission and ferroelectric exciton ordering near Mott insulating

- state in WSe_2/WS_2 heterobilayers, *Nature Materials*, **1** (2026).
- [32] S. Miao, T. Wang, X. Huang, D. Chen, Z. Lian, C. Wang, M. Blei, T. Taniguchi, K. Watanabe, S. Tongay, Z. Wang, D. Xiao, Y.-T. Cui, and S.-F. Shi, Strong interaction between interlayer excitons and correlated electrons in WSe_2/WS_2 moiré superlattice, *Nature Communications* **12**, 3608 (2021).
- [33] J. Kim, J. Park, H. Choi, T. Kim, S. Cha, Y. Lee, K. Watanabe, T. Taniguchi, J. Kim, M.-H. Jo, and H. Choi, Correlation-driven nonequilibrium exciton site transition in a WSe_2/WS_2 moiré supercell, *Nature Communications* **15**, 3312 (2024).
- [34] X. Wang, X. Zhang, J. Zhu, H. Park, Y. Wang, C. Wang, W. G. Holtzmann, T. Taniguchi, K. Watanabe, J. Yan, D. R. Gamelin, W. Yao, D. Xiao, T. Cao, and X. Xu, Intercell moiré exciton complexes in electron lattices, *Nature Materials* **22**, 599 (2023), 2206.08424.
- [35] D. Chen, Z. Lian, X. Huang, Y. Su, M. Rashetnia, L. Yan, M. Blei, T. Taniguchi, K. Watanabe, S. Tongay, Z. Wang, C. Zhang, Y.-T. Cui, and S.-F. Shi, Tuning moiré excitons and correlated electronic states through layer degree of freedom, *Nature Communications* **13**, 4810 (2022).
- [36] D. Xiao, G.-B. Liu, W. Feng, X. Xu, and W. Yao, Coupled spin and valley physics in monolayers of MoS_2 and other group-VI dichalcogenides, *Physical Review Letters* **108**, 196802 (2012), 1112.3144.
- [37] K. F. Mak, K. He, J. Shan, and T. F. Heinz, Control of valley polarization in monolayer MoS_2 by optical helicity, *Nature Nanotechnology* **7**, 494 (2012), 05, 1205.1822.
- [38] X. Xu, W. Yao, D. Xiao, and T. F. Heinz, Spin and pseudospins in layered transition metal dichalcogenides, *Nature Physics* **10**, 343 (2014).
- [39] H. Yu, G.-B. Liu, and W. Yao, Brightened spin-triplet interlayer excitons and optical selection rules in van der Waals heterobilayers, *2D Materials* **5**, 035021 (2018), 1803.01292.
- [40] T. Wang, S. Miao, Z. Li, Y. Meng, Z. Lu, Z. Lian, M. Blei, T. Taniguchi, K. Watanabe, S. Tongay, D. Smirnov, and S.-F. Shi, Giant valley-Zeeman splitting from spin-singlet and spin-triplet interlayer excitons in $\text{WSe}_2/\text{MoSe}_2$ heterostructure, *Nano Letters* **20**, 694 (2020), 1912.11885.
- [41] P. Eickholt, C. Sanders, M. Dendzik, L. Bignardi, D. Lizzit, S. Lizzit, A. Bruix, P. Hofmann, and M. Donath, Spin structure of K valleys in single-layer WS_2 on $\text{Au}(111)$, *Physical Review Letters* **121**, 136402 (2018), 1807.11235.
- [42] M. A. U. Absor, H. Kotaka, F. Ishii, and M. Saito, Strain-controlled spin splitting in the conduction band of monolayer WS_2 , *Physical Review B* **94**, 115131 (2016), 1607.07566.
- [43] K. Kośmider, J. W. González, and J. Fernández-Rossier, Large spin splitting in the conduction band of transition metal dichalcogenide monolayers, *Physical Review B* **88**, 245436 (2013), 1311.0049.
- [44] J. Wang, J. Ardelean, Y. Bai, A. Steinhoff, M. Florian, F. Jahnke, X. Xu, M. Kira, J. Hone, and X.-Y. Zhu, Optical generation of high carrier densities in 2D semiconductor heterobilayers, *Science Advances* **5**, eaax0145 (2019).
- [45] A. Ciarrocchi, D. Unuchek, A. Avsar, K. Watanabe, T. Taniguchi, and A. Kis, Polarization switching and electrical control of interlayer excitons in two-dimensional van der Waals heterostructures, *Nature Photonics* **13**, 131 (2019), 1803.06405.
- [46] D. MacNeill, C. Heikes, K. F. Mak, Z. Anderson, A. Kormányos, V. Zólyomi, J. Park, and D. C. Ralph, Breaking of valley degeneracy by magnetic field in monolayer MoSe_2 , *Physical Review Letters* **114**, 037401 (2014), 1407.0686.
- [47] Y.-C. Wu, M. DeCapua, Z. Xu, T. Taniguchi, K. Watanabe, Y. Shi, and J. Yan, Highly tunable valley polarization of potential-trapped moiré excitons in WSe_2/WS_2 heterojunctions, *Physical Review Letters* **134**, 256402 (2025).
- [48] M. Brotons-Gisbert, H. Baek, A. Molina-Sánchez, A. Campbell, E. Scerri, D. White, K. Watanabe, T. Taniguchi, C. Bonato, and B. D. Gerardot, Spin-layer locking of interlayer excitons trapped in moiré potentials, *Nature Materials* **19**, 630 (2020), 1908.03778.
- [49] W. Li, X. Lu, J. Wu, and A. Srivastava, Optical control of the valley Zeeman effect through many-exciton interactions, *Nature Nanotechnology* **16**, 148 (2021), 2006.03061.
- [50] T. Yu and M. W. Wu, Valley depolarization due to intervalley and intravalley electron-hole exchange interactions in monolayer MoS_2 , *Physical Review B* **89**, 205303 (2014), 1401.0047.
- [51] C. Jin, E. Y. Ma, O. Karni, E. C. Regan, F. Wang, and T. F. Heinz, Ultrafast dynamics in van der Waals heterostructures, *Nature Nanotechnology* **13**, 994 (2018).
- [52] Y. Jiang, S. Chen, W. Zheng, B. Zheng, and A. Pan, Interlayer exciton formation, relaxation, and transport in TMD van der Waals heterostructures, *Light: Science & Applications* **10**, 72 (2021), 09.
- [53] G. Aivazian, Z. Gong, A. M. Jones, R.-L. Chu, J. Yan, D. G. Mandrus, C. Zhang, D. Cobden, W. Yao, and X. Xu, Magnetic control of valley pseudospin in monolayer WSe_2 , *Nature Physics* **11**, 148 (2015), 1407.2645.
- [54] Y. Jiang, Y. She, X. Cheng, Q. Tan, J. Yang, Y. Zhao, P. Liu, M. Wu, X. Dai, Z. Wang, H. Cai, N. Pan, and X. Wang, Tuning valley polarization of moiré-trapped biexcitons by fine-structure occupation in WS_2/WSe_2 heterostructures, *Nature Communications* **17**, 1089 (2025).
- [55] J. Zhu, H. Zheng, X. Wang, H. Park, C. Xiao, Y. Zhang, T. Taniguchi, K. Watanabe, J. Yan, D. R. Gamelin, W. Yao, and X. Xu, Moiré exchange effect in twisted WSe_2/WS_2 heterobilayer, *Physical Review Letters* **133**, 086501 (2024).
- [56] A. J. Campbell, M. Brotons-Gisbert, H. Baek, V. Vitale, T. Taniguchi, K. Watanabe, J. Lischner, and B. D. Gerardot, Exciton-polarons in the presence of strongly correlated electronic states in a $\text{MoSe}_2/\text{WSe}_2$ moiré superlattice, *npj 2D Materials and Applications* **6**, 79 (2022), 32.

Supplemental Material for
“Unveiling the Spin–Valley Structure of Dipolar Exciton Ladders
in R-stacked WSe₂/WS₂ Moiré Heterobilayers”

Byeong Wook Cho,^{1,*} Tatyana V. Ivanova,^{1,*} Zhe Li,¹ Takashi Taniguchi,²
Kenji Watanabe,³ Brian D. Gerardot,¹ and Mauro Brotons-Gisbert¹

¹*Institute of Photonics and Quantum Sciences,
SUPA, Heriot-Watt University, Edinburgh, UK*

²*Research Center for Materials Nanoarchitectonics,
National Institute for Materials Science,
1-1 Namiki, Tsukuba 305-0044, Japan*

³*Research Center for Electronic and Optical Materials,
National Institute for Materials Science,
1-1 Namiki, Tsukuba 305-0044, Japan*

(Dated: July 9, 2026)

S1. DEVICE FABRICATION AND TWIST-ANGLE DETERMINATION

The R-stacked WSe_2/WS_2 moiré heterobilayer devices were fabricated using a dry-transfer pickup technique. Monolayer WSe_2 , monolayer WS_2 , few-layer hBN, and graphite flakes were mechanically exfoliated from bulk crystals and identified by optical contrast. The monolayer nature of the TMD flakes was further confirmed by photoluminescence (PL) measurements. The heterostructures were assembled using a polycarbonate (PC)/PDMS stamp. The WSe_2 and WS_2 monolayers were sequentially picked up together with hBN flakes while controlling their relative orientation to obtain R-type stacking with small twist angles. The completed stack was released onto a prepatterned electrode substrate by heating the PC film at 200°C , followed by removal of residual PC in chloroform.

The crystallographic orientations of the WSe_2 and WS_2 monolayers were first estimated from straight crystal edges and then verified by polarization-resolved second-harmonic generation (SHG) measurements. Figure S1 shows optical microscope images of devices R1–R3 together with the corresponding SHG polar plots measured from the WSe_2 and WS_2 monolayers.

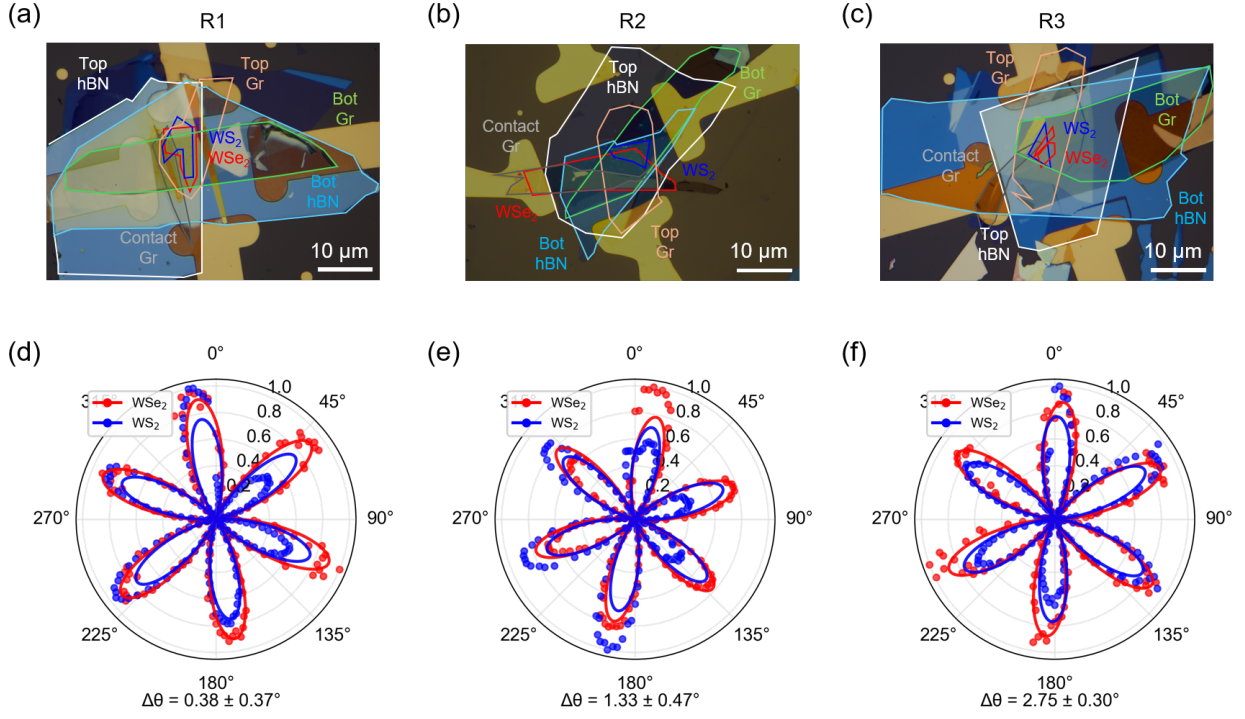


FIG. S1. Device images and polarization-resolved SHG characterization of R-stacked WSe_2/WS_2 moiré heterobilayers. (a)–(c) Optical microscope images of devices R1–R3. (d)–(f) Corresponding SHG polar plots of the WSe_2 and WS_2 monolayers. The extracted twist angles are $0.38 \pm 0.37^\circ$, $1.33 \pm 0.47^\circ$, and $2.75 \pm 0.30^\circ$ for R1, R2, and R3, respectively.

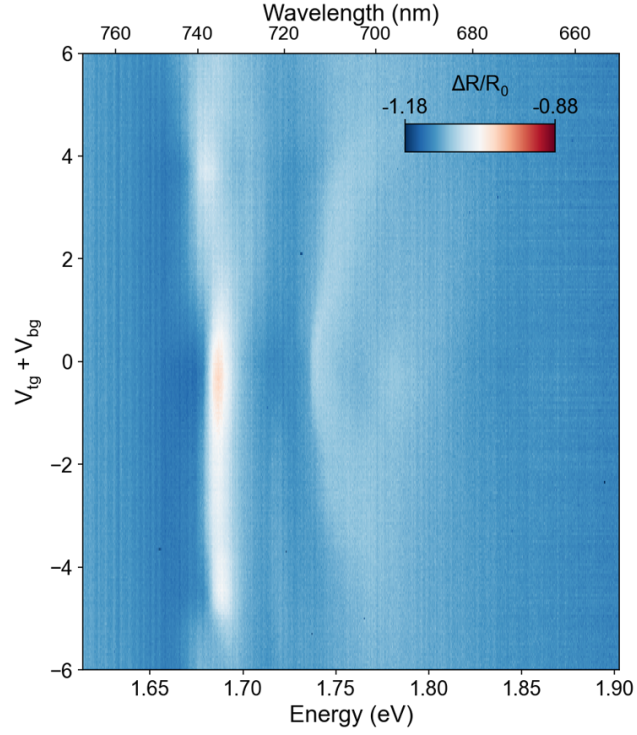


FIG. S2. Reflectance contrast of device R1 near the WSe_2 intralayer exciton resonance. The main WSe_2 $1s$ resonance appears at approximately 1.680 eV, accompanied by higher-energy moiré-induced spectral features.

S2. CAPACITANCE MODEL

The carrier density and out-of-plane electric field in the dual-gated WSe_2/WS_2 moiré heterobilayer devices were estimated using a parallel-plate capacitance model. The top and bottom graphite gates are separated from the WSe_2/WS_2 heterobilayer by hBN dielectric layers with thicknesses d_t and d_b , respectively. For device R1, both the top and bottom hBN thicknesses are approximately 40 nm. Taking the gate voltages relative to the charge-neutrality point, the induced carrier density is given by

$$n = \frac{\epsilon_0 \epsilon_{\text{hBN}}}{e} \left(\frac{V_{\text{tg}}}{d_t} + \frac{V_{\text{bg}}}{d_b} \right), \quad (\text{S1})$$

where $\epsilon_0 = 8.854 \times 10^{-12}$ F/m is the vacuum permittivity, $\epsilon_{\text{hBN}} \approx 3.8$ is the relative dielectric constant of hBN, and e is the elementary charge.

The out-of-plane electric field is estimated from the difference between the top- and bottom-gate displacement fields:

$$E_z = \frac{\epsilon_{\text{hBN}}}{2} \left(\frac{V_{\text{tg}}}{d_t} - \frac{V_{\text{bg}}}{d_b} \right). \quad (\text{S2})$$

This dual-gate geometry allows the carrier density and vertical electric field to be tuned independently by sweeping V_{tg} and V_{bg} along appropriate trajectories in gate-voltage space.

S3. OPTICAL SELECTION RULE

In R-stacked WSe₂/WS₂ heterobilayers, the K valleys of WSe₂ and WS₂ are nearly momentum-aligned, as are the corresponding $-K$ valleys. The moiré-trapped IXs considered here are localized at the R_h^X site, so their emission helicity is determined by the spin-valley indices of the electron and hole involved in recombination. The optical selection rules for interband transitions at the relevant local registries are summarized in Table S1.

Following the convention in Table S1, the $+K$ and $-K$ valley triplet transitions at the R_h^X site couple predominantly to σ^+ and σ^- polarized light, respectively, whereas the corresponding singlet transitions couple to the opposite helicities, σ^- and σ^+ , respectively. These selection rules provide the basis for assigning the spin-valley character of the IX peaks in the main text.

TABLE S1. Optical selection rules for interband transitions at different local registries in R-stacked WSe₂/WS₂, adapted from [1]

Transition	R_h^h	R_h^M	R_h^X
$ K_v \uparrow\rangle \rightarrow K'_c \uparrow\rangle$	σ_+	z	σ_-
$ K_v \uparrow\rangle \rightarrow K'_c \downarrow\rangle$	z	σ_-	σ_+
$ -K_v \downarrow\rangle \rightarrow -K'_c \downarrow\rangle$	σ_-	z	σ_+
$ -K_v \downarrow\rangle \rightarrow -K'_c \uparrow\rangle$	z	σ_+	σ_-

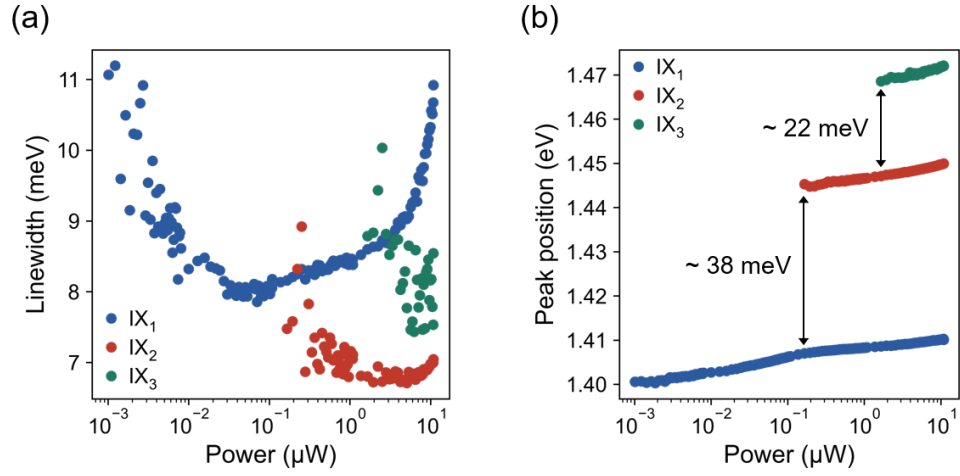


FIG. S3. Power-dependent PL peak parameters of device R1 at charge neutrality. (a) Extracted linewidths and (b) peak energies of IX_1 , IX_2 , and IX_3 as a function of excitation power.

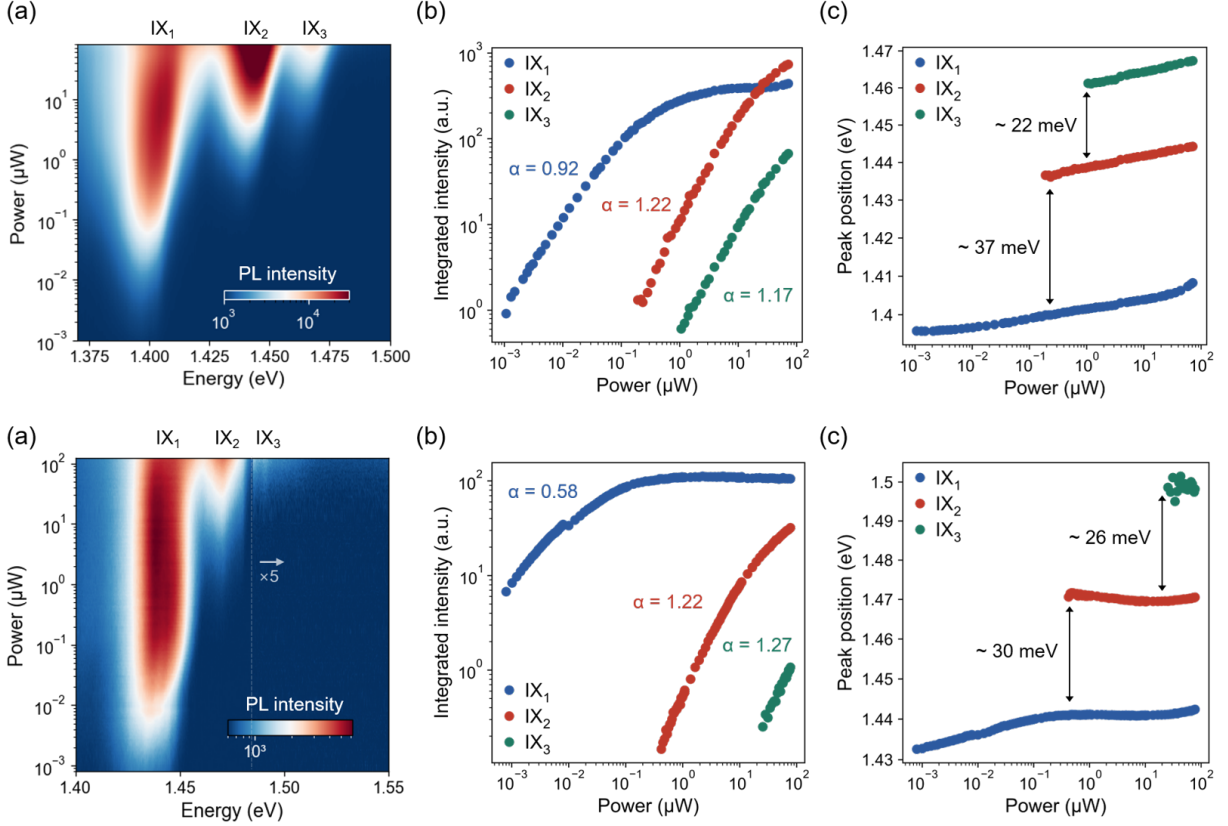


FIG. S4. Power-dependent PL measurements of additional R-stacked WSe_2/WS_2 moiré heterobilayer devices. (a)–(c) Data from device R2: power-dependent PL map, integrated PL intensities, and peak energies of IX_1 , IX_2 , and IX_3 . (d)–(f) Corresponding data from device R3. The emergence of higher-energy IX_2 and IX_3 peaks at elevated excitation powers, together with their nonlinear power dependence, is consistent with the behavior observed in device R1.

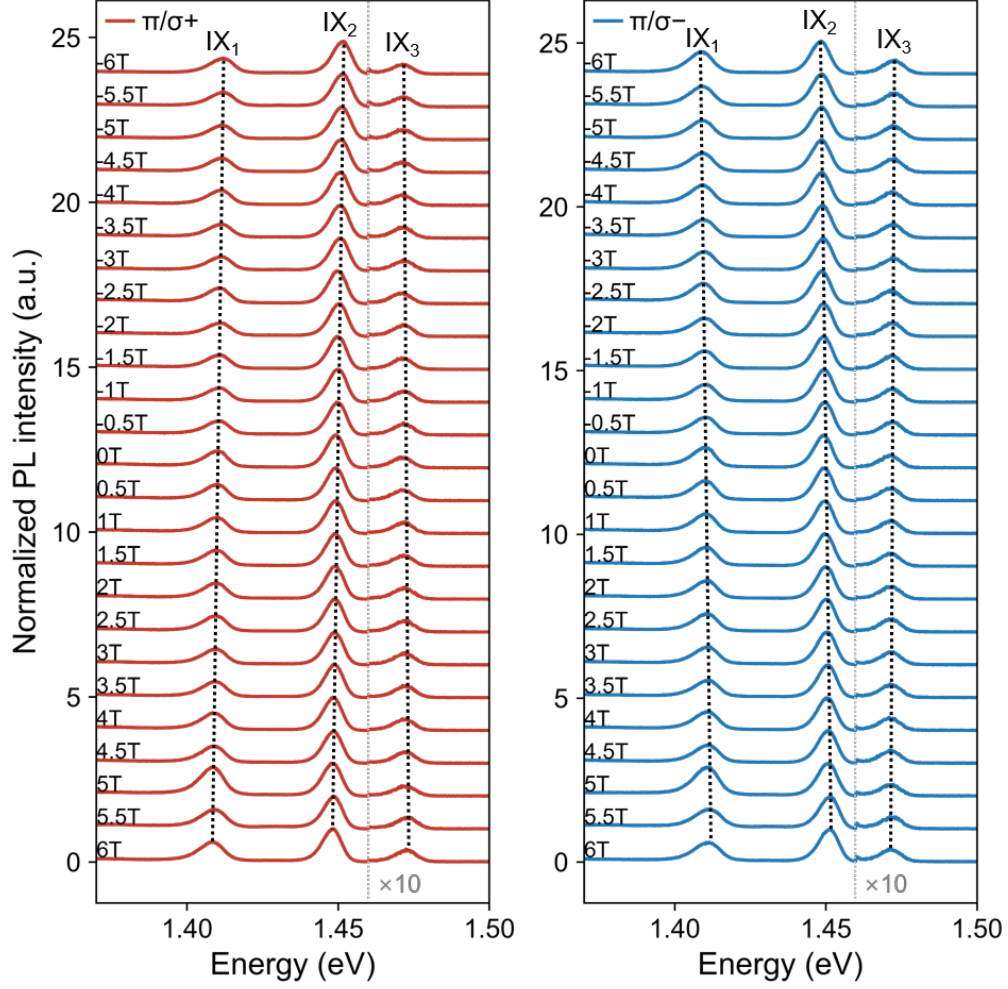


FIG. S5. Helicity-resolved magneto-PL spectra of device R1 at charge neutrality under linearly polarized 1.72 eV excitation. (a) PL spectra detected in the σ^+ channel. (b) PL spectra detected in the σ^- channel. The out-of-plane magnetic field was swept from -6 T to $+6$ T in steps of 0.5 T. The IX_3 emission is magnified by a factor of 10 for clarity.

S4. g -FACTOR CALCULATION

The effective exciton g -factors were extracted from helicity-resolved magneto-PL measurements (see Fig. S5). For each magnetic field, the PL spectra collected in the σ^+ and σ^- detection channels were fitted with Gaussian functions to determine the peak energies $E_{\sigma^+}(B)$ and $E_{\sigma^-}(B)$. The Zeeman splitting was then defined as

$$\Delta E_Z(B) = E_{\sigma^+}(B) - E_{\sigma^-}(B). \quad (\text{S3})$$

The magnetic-field dependence of the Zeeman splitting was fitted using

$$\Delta E_Z(B) = g\mu_B B, \quad (\text{S4})$$

where $\mu_B = 57.88 \mu\text{eV}/\text{T}$ is the Bohr magneton and g is the effective exciton g -factor. The g -factor was obtained from the slope of the linear fit,

$$g = \frac{1}{\mu_B} \frac{d\Delta E_Z}{dB}. \quad (\text{S5})$$

The sign of g is determined by the relative energy shift of the σ^+ and σ^- emission components with magnetic field. Positive and negative values therefore indicate opposite valley-Zeeman responses of the corresponding IX states.

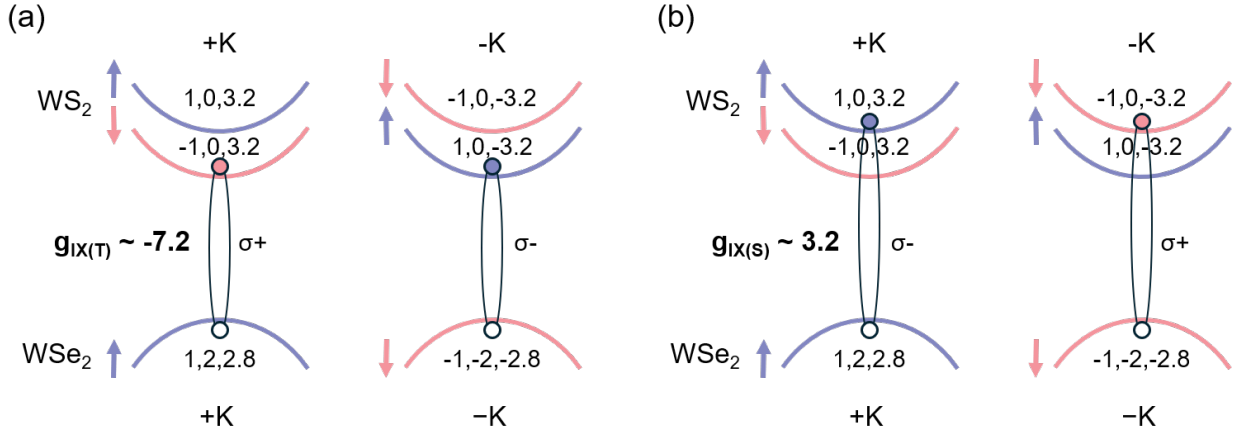


FIG. S6. Schematic illustration of the contributions to the valley-Zeeman response of interlayer exciton transitions. (a) Spin-triplet transition and (b) spin-singlet transition considered for the effective g -factor estimation. The magnetic-field-induced energy shift of the conduction or valence band edge is decomposed as $\Delta E_{c/v} = \Delta_s + \Delta_a + \Delta_v$, where Δ_s is the spin contribution, Δ_a is the atomic orbital contribution, and Δ_v is the valley magnetic moment contribution associated with the Berry curvature. The numerical labels indicate the representative spin, atomic orbital, and valley contributions used to estimate the effective Zeeman response of each transition. The Berry-curvature-related valley contributions were taken from [2].

S5. POLARIZATION CALIBRATION

To obtain reliable degrees of circular polarization, we calibrated the polarization-dependent response of the optical setup. In polarization-resolved PL measurements, the measured intensity can be affected not only by the sample emission but also by helicity-dependent transmission or detection efficiency of the optical path. This artificial asymmetry can arise from polarization-dependent reflection and transmission of optical components, most likely the beam splitter in our setup.

The calibration procedure is illustrated in Fig. S7. A reference laser signal was sent through the collection path, and the detected intensity was recorded while rotating the half-wave plate in the collection arm. In an ideal polarization-independent detection path, the measured intensity should remain constant as the analyzer angle is varied. Instead, we observed a weak angular modulation of the detected intensity, indicating a finite polarization-dependent response of the setup.

The measured modulation curve was used as a calibration factor for the helicity-resolved PL spectra. The raw σ^+ and σ^- intensities were corrected by the corresponding detection efficiencies before calculating the degree of circular polarization,

$$\rho = \frac{I_{\sigma^+} - I_{\sigma^-}}{I_{\sigma^+} + I_{\sigma^-}}. \quad (\text{S6})$$

This procedure removes setup-induced polarization asymmetry and allows the extracted polarization values to reflect the intrinsic helicity response of the IX emission.

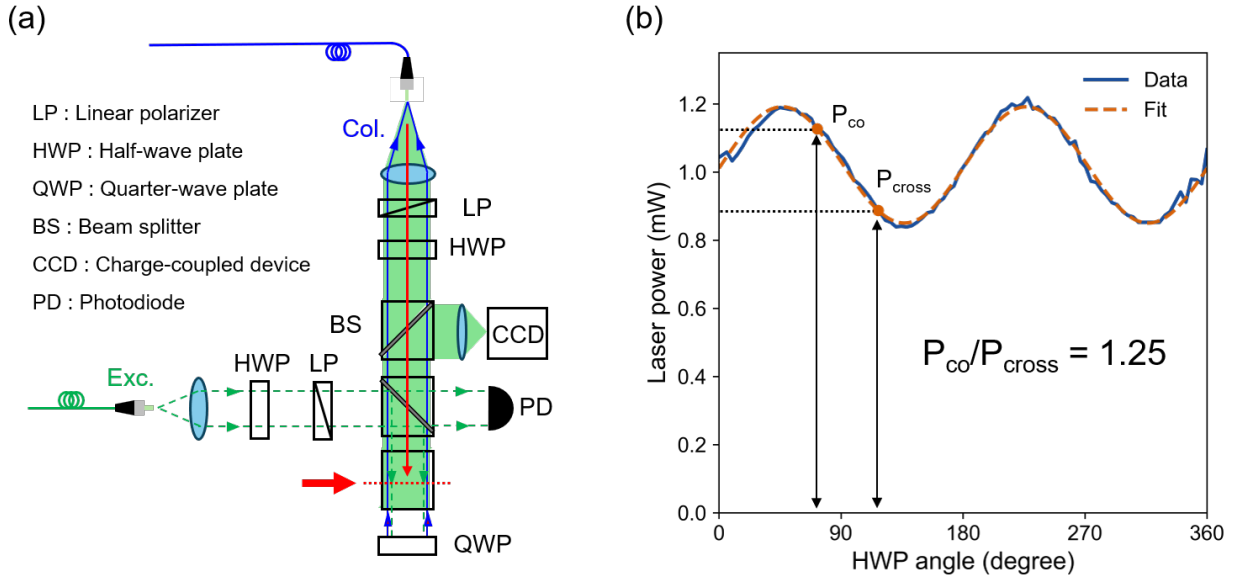


FIG. S7. Optical setup and polarization calibration. (a) Schematic of the excitation and collection paths used for helicity-resolved PL measurements, showing the polarization-control and polarization-analysis optics. A reference laser signal was sent through the collection path, and the detected intensity was recorded while rotating the half-wave plate in the collection arm. (b) Measured angular dependence of the reference signal, together with a sinusoidal fit. The observed modulation reflects the polarization-dependent response of the optical setup, mainly arising from the beam splitters. This calibration curve was used to correct the raw σ^+ and σ^- PL intensities.

S6. EXCHANGE INTERACTION

The magnetic-field dependence of the degree of circular polarization provides an estimate of the exchange-interaction strength [3–5]. The first panel of Fig. 3(d) in the main text and the power-dependent data shown in Fig. S8 were fitted using the following model:

$$\rho(B) = \frac{\rho_0}{1 + \frac{2\tau/\tau_{v0}}{1 + (B/B_c)^2}}, \quad (\text{S7})$$

where ρ_0 is the initial degree of circular polarization in the absence of valley depolarization, τ_{v0} is the valley depolarization time at zero magnetic field, and τ is the exciton lifetime. The characteristic magnetic field B_c represents the field scale at which the out-of-plane magnetic field suppresses exchange-driven valley depolarization, and therefore provides an estimate of the exchange-interaction strength.

Following previous reports [4, 5], we estimate the corresponding exchange-energy scale as

$$\Delta_{\text{ex}} \sim |g|\mu_B B_c, \quad (\text{S8})$$

where $\mu_B = 57.88 \mu\text{eV}/\text{T}$ is the Bohr magneton and g is the effective exciton g -factor. Using the measured value $|g| = 8.73$ for IX₁, the extracted characteristic fields $B_c = 0.05, 0.04,$ and 0.03 T at excitation powers of 30, 150, and 500 nW correspond to $\Delta_{\text{ex}} \approx 0.025, 0.020,$ and 0.015 meV , respectively.

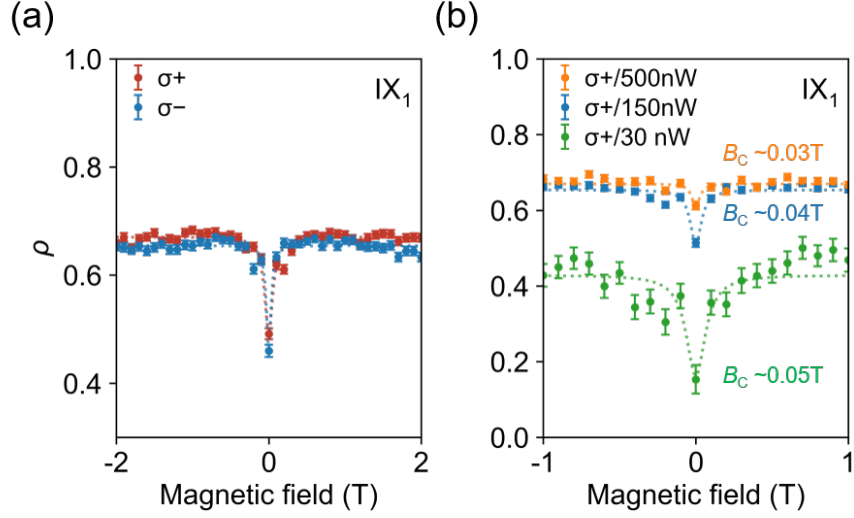


FIG. S8. Magnetic-field dependence of the degree of circular polarization of IX₁. (a) Full-range polarization data under σ^+ and σ^- excitation, extending the field range shown in Fig. 3(d). (b) Power-dependent polarization data fitted to extract the characteristic field B_c for the rapid polarization increase. The extracted B_c values remain similar, $\sim 0.03\text{--}0.05\text{ T}$, across the investigated excitation-power range, while a residual depolarization persists even at high magnetic fields.

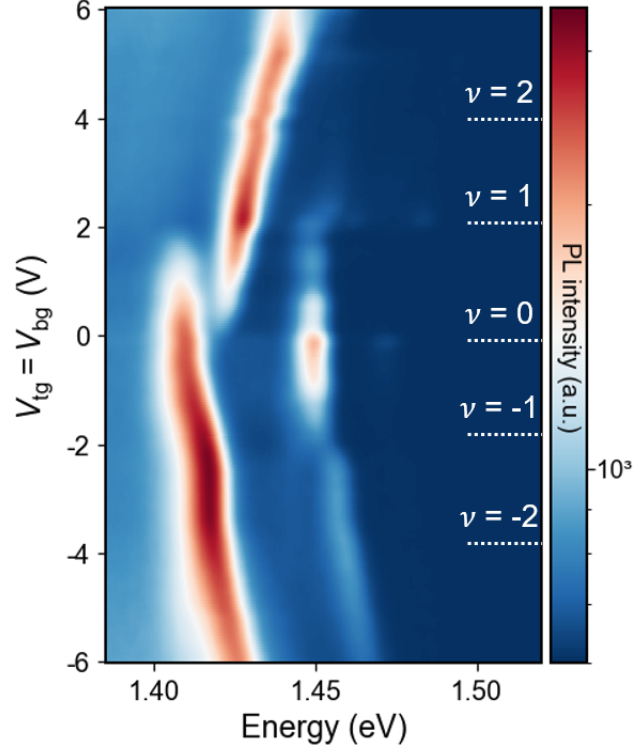


FIG. S9. Full filling-dependent PL spectra of device R1 measured at an excitation power of $7 \mu\text{W}$. Dashed lines indicate representative integer filling factors $\nu = -2, -1, 0, 1,$ and 2 . The zoomed-in range between $\nu = -1$ and $\nu = 1$ is discussed in Fig. 4(a).

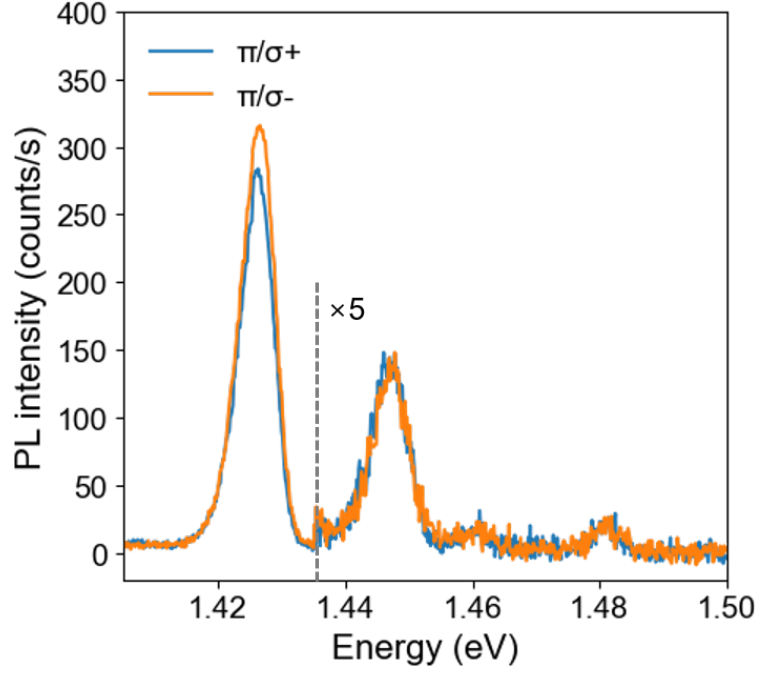


FIG. S10. Helicity-resolved PL spectra of device R1 at $\nu = 1$ under linearly polarized excitation. The σ^+ and σ^- detection channels show no clear circular polarization or helicity-dependent splitting, confirming that the splitting of IX'_2 in Fig. 4(d) is induced by circularly polarized excitation.

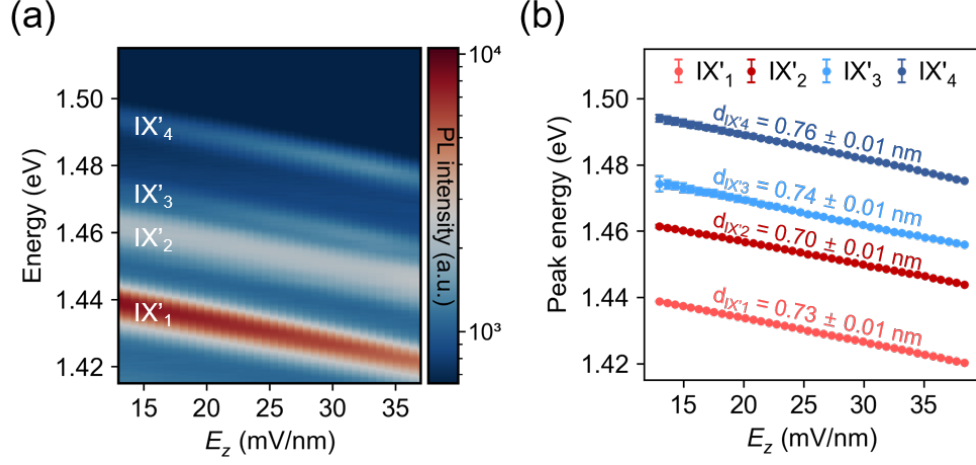


FIG. S11. Out-of-plane electric-field dependence of IX'_1 – IX'_4 at $\nu = 1$. (a) PL spectra as a function of vertical electric field. (b) Extracted peak energies with linear Stark-shift fits. The fitted electron–hole separations are similar for all four peaks, $d \sim 0.7$ nm, indicating that IX'_1 – IX'_4 originate from the same moiré site.

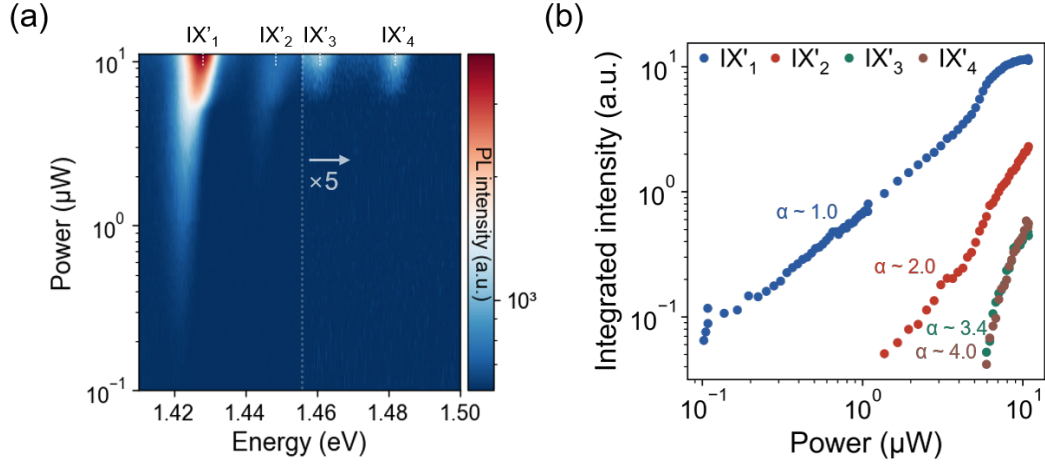


FIG. S12. Excitation-power dependence of the electron-doped IX peaks at $\nu = 1$. (a) Power-dependent PL map showing the emergence of IX'_1 – IX'_4 . The high-energy spectral region containing IX'_3 and IX'_4 is magnified by a factor of 5 for clarity. (b) Integrated PL intensities of IX'_1 – IX'_4 as a function of excitation power, plotted on a log–log scale. The extracted power-law exponents are $\alpha \sim 1.0$, 2.0, 3.4, and 4.0 for IX'_1 , IX'_2 , IX'_3 , and IX'_4 , respectively.

S7. DIPOLAR LADDERS IN WSe₂/WS₂ AT $\nu = -1$

We further examined the dipolar IX emission in the hole-doped regime. Figure S13(a) shows the PL spectrum at $\nu = -1$, where three emission features are observed and denoted IX₁⁺, IX₂⁺, and IX₃⁺. Here, the superscript + indicates features observed in the hole-doped regime.

In contrast to the electron-doped side, where a distinct charged exciton-carrier complex IX'₁ emerges above IX₁, hole doping mainly produces a weak blueshift of the IX₁ emission. This weaker spectral response may be related to the smaller energy scale expected for hole-hole repulsion compared with electron-electron repulsion in R-stacked WSe₂/WS₂ moiré heterobilayers [6]. Thus, IX₁⁺ can be viewed as the hole-doped counterpart of IX₁, but we do not observe a clearly separated polaron-like exciton-carrier resonance analogous to IX'₁.

The behavior of the two-IX emission also differs from that of IX₁⁺. As the hole filling increases, the IX₂ emission gradually loses oscillator strength while its peak energy remains nearly unchanged. Near $\nu = -1$, two adjacent higher-energy peaks are resolved and denoted IX₂⁺ and IX₃⁺. The nearly fixed energy of IX₂⁺ suggests that this feature retains the character of the charge-neutral IX₂^(T,T) emission, similar to the electron-doped counterpart IX'₂ discussed in the main text. By contrast, IX₃⁺ blueshifts with increasing hole doping by an amount comparable to that of IX₁⁺, as shown in Fig. S13(b). This behavior suggests that IX₃⁺ may be associated with a hole-dressed two-IX emission.

The spin-valley character of these hole-doped features was further examined using helicity-resolved magneto-PL measurements (Fig. S13(c)). The extracted Zeeman splittings show that IX₁⁺, IX₂⁺, and IX₃⁺ all exhibit triplet-like magnetic responses, indicating that the observed hole-doped features are primarily derived from IX^(T) transitions. Overall, these measurements show that hole doping modifies the dipolar ladder mainly through weak energy shifts and redistribution of oscillator strength, without producing the pronounced electron-induced reconstruction observed near $\nu = 1$.

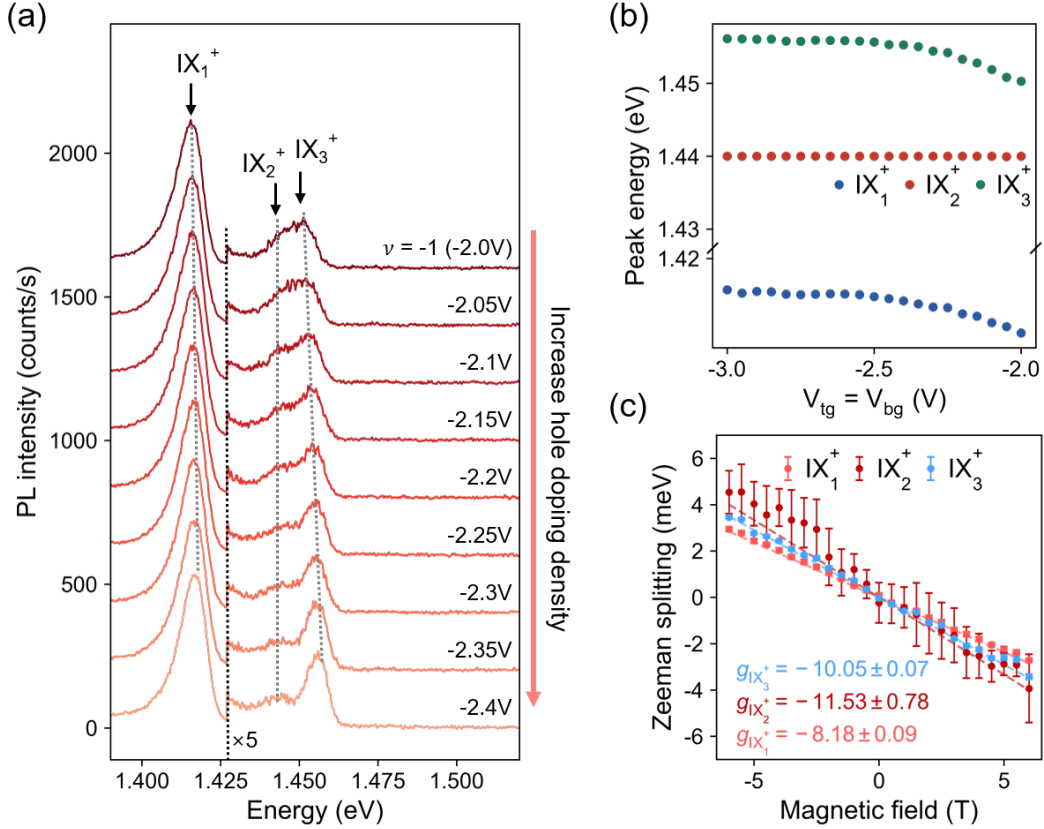


FIG. S13. Dipolar ladders at $\nu = -1$ and in the hole-doped regime. (a) PL spectra showing the evolution of IX_1^+ , IX_2^+ , and IX_3^+ as the hole filling is increased beyond $\nu = -1$. The arrow indicates increasing hole doping. (b) Extracted peak energies of IX_1^+ , IX_2^+ , and IX_3^+ as a function of hole filling. IX_1^+ and IX_3^+ show comparable blueshifts, whereas IX_2^+ remains nearly fixed in energy. (c) Zeeman splittings of IX_1^+ , IX_2^+ , and IX_3^+ extracted from helicity-resolved magneto-PL measurements, together with linear fits. The extracted g -factors for all three-hole doped emission features are consistent with those of triplet-IX transition.

* These authors contributed equally to this work.

- [1] X. Wang, X. Zhang, J. Zhu, H. Park, Y. Wang, C. Wang, W. G. Holtzmann, T. Taniguchi, K. Watanabe, J. Yan, D. R. Gamelin, W. Yao, D. Xiao, T. Cao, and X. Xu, Intercell moiré exciton complexes in electron lattices, *Nature Materials* **22**, 599 (2023), 2206.08424.
- [2] A. Kormányos, G. Burkard, M. Gmitra, J. Fabian, V. Zólyomi, N. D. Drummond, and V. Fal'ko, $k \cdot p$ theory for two-dimensional transition metal dichalcogenide semiconductors, *2D Materials*

- 2**, 049501 (2015).
- [3] Y. She, Y. Jiang, J. Yang, Y. Zhao, P. Liu, M. Wu, X. Dai, Z. Wang, X. Cheng, H. Cai, N. Pan, and X. Wang, Magneto-polarization controlled by intervalley scattering of interlayer excitons and carriers in WS_2/WSe_2 heterostructure, *Nano Letters* **25**, 6708 (2025).
- [4] Y.-C. Wu, M. DeCapua, Z. Xu, T. Taniguchi, K. Watanabe, Y. Shi, and J. Yan, Highly tunable valley polarization of potential-trapped moiré excitons in WSe_2/WS_2 heterojunctions, *Physical Review Letters* **134**, 256402 (2025).
- [5] Y. Jiang, Y. She, X. Cheng, Q. Tan, J. Yang, Y. Zhao, P. Liu, M. Wu, X. Dai, Z. Wang, H. Cai, N. Pan, and X. Wang, Tuning valley polarization of moiré-trapped biexcitons by fine-structure occupation in WS_2/WSe_2 heterostructures, *Nature Communications* **17**, 1089 (2025).
- [6] Z. Lian, Y. Meng, L. Ma, I. Maity, L. Yan, Q. Wu, X. Huang, D. Chen, X. Chen, X. Chen, M. Blei, T. Taniguchi, K. Watanabe, S. Tongay, J. Lischner, Y.-T. Cui, and S.-F. Shi, Valley-polarized excitonic Mott insulator in WS_2/WSe_2 moiré superlattice, *Nature Physics* **20**, 34 (2024).